

Structure, Hydrogen Storage, and Electrochemical Properties of Body-Centered-Cubic $Ti_{40}V_{30}Cr_{15}Mn_{13}X_2$ Alloys ($X = B, Si, Mn, Ni, Zr, Nb, Mo, \text{ and } La$)

Kwo-Hsiung Young ^{1,2,*}, Taihei Ouchi ², Baoquan Huang ² and Jean Nei ²

¹ Department of Chemical Engineering and Materials Science, Wayne State University, Detroit, MI 48202, USA

² BASF/Battery Materials-Ovonic, 2983 Waterview Drive, Rochester Hills, MI 48309, USA;
E-Mails: taihei.ouchi@basf.com (T.O.); baoquang.huang@basf.com (B.H.); jean.nei@basf.com (J.N.)

* Author to whom correspondence should be addressed; E-Mail: kwo.young@basf.com;
Tel.: +1-248-293-7000; Fax: +1-248-299-4228.

Academic Editor: Andreas Jossen

Received: 2 November 2015 / Accepted: 4 December 2015 / Published: 10 December 2015

Abstract: Structure, gaseous phase hydrogen storage, and electrochemical properties of a series of TiVCrMn-based body-centered-cubic (BCC) alloys with different partial substitutions for Mn with covalent elements (B and Si), transition metals (Ni, Zr, Nb, and Mo), and rare earth element (La) were investigated. Although the influences from substitutions on structure and gaseous phase storage properties were minor, influences on electrochemical discharge capacity were significant. The first cycle capacity ranged from 16 $mA\cdot h\cdot g^{-1}$ (Si-substituted) to 247 $mA\cdot h\cdot g^{-1}$ (Mo-substituted). Severe alloy passivation in 30% KOH electrolyte was observed, and an original capacity close to 500 $mA\cdot h\cdot g^{-1}$ could possibly be achieved by Mo-substituted alloy if a non-corrosive electrolyte was employed. Surface coating of Nafion to the Mo-substituted alloy was able to increase the first cycle capacity to 408 $mA\cdot h\cdot g^{-1}$, but the degradation rate in $mA\cdot h\cdot g^{-1}\cdot cycle^{-1}$ was still similar to that of standard testing. Electrochemical capacity was found to be closely related to BCC phase unit cell volume and width of the an extra small pressure plateau at around 0.3 MPa on the 30 °C pressure-concentration-temperature (PCT) desorption isotherm. Judging from its high electrochemical discharge capacity, Mo was the most beneficial substitution in BCC alloys for Ni/metal hydride (MH) battery application.

Keywords: hydrogen absorbing alloys; metal hydride (MH) electrode; laves phase alloys; body-centered-cubic (BCC) alloys; catalytic phase

1. Introduction

Among all metal hydride (MH) alloy families, body-centered-cubic (BCC) solid solution alloy has the highest reversible hydrogen storage at ambient temperature. Although its gaseous phase hydrogen storage capacity is very high (up to 4.0 wt%, equivalent to $1072 \text{ mAh}\cdot\text{g}^{-1}$ [1]), few electrochemical studies have been performed on the pure BCC phase MH alloy due to its strong metal-hydrogen bonding and low surface reaction activity [2–5]. Inoue and his coworker reported a $\text{TiV}_{3.4}\text{Ni}_{0.6}$ alloy achieving $360 \text{ mAh}\cdot\text{g}^{-1}$ at room temperature with a discharge rate of $50 \text{ mA}\cdot\text{g}^{-1}$ [3]. Mori and Iba improved both the capacity and cycle stability by adding Y, lanthanoids, Pd, or Pt into a TiCrVNi BCC alloy and reached $462 \text{ mAh}\cdot\text{g}^{-1}$ [4]. Yu and his coworker reported a $\text{Ti}_{40}\text{V}_{30}\text{Cr}_{15}\text{Mn}_{15}$ alloy with an initial capacity of $814 \text{ mAh}\cdot\text{g}^{-1}$ measured with a rate of $10 \text{ mA}\cdot\text{g}^{-1}$ at 80°C ; however, degradation was high due to surface cracking, preferential leaching of V into the KOH electrolyte, and formation of TiO_x on the surface that further blocks electrochemical reaction [5]. One or more secondary phases, such as C14, C15, and/or B2, with a high grain boundary density was introduced to improve the absorption kinetics [6], facilitate formation due to its brittleness [7–9], and increase the surface catalytic activity [10–15] by enhancing the synergistic effect between the main and secondary phases. High phase boundary density also promotes the formation of coherent and catalytic interfaces between the BCC and secondary phases and, therefore, improves hydrogen absorption and desorption kinetics [16].

In this experiment, we focus on continuing the work on $\text{Ti}_{40}\text{V}_{30}\text{Cr}_{15}\text{Mn}_{15}$ alloy with an electrochemical study performed at room temperature and an examination of substitution effects from covalent elements, transition metals, and rare-earth elements on structure, gaseous phase, and electrochemical properties. The alloy formula in the current study can be summarized as $\text{Ti}_{40}\text{V}_{30}\text{Cr}_{15}\text{Mn}_{13}X_2$, where $X = \text{B}, \text{Si}, \text{Mn}, \text{Ni}, \text{Zr}, \text{Nb}, \text{Mo}$, and La .

2. Experimental Setup

In this experiment, an arc melting technique was chosen for the sample preparation. The ingot size was about 12 g and the melting was performed in an Ar environment. A Varian Liberty 100 inductively-coupled plasma optical emission spectrometer (ICP-OES, Agilent Technologies, Santa Clara, CA, USA) was used to verify the chemical composition of the ingot comparing to the ratios in the raw materials. A Philips X’Pert Pro X-ray diffractometer (XRD, Philips, Amsterdam, The Netherlands) was used to study the microstructure, and a JEOL-JSM6320F scanning electron microscope (SEM, JEOL, Tokyo, Japan) with energy dispersive spectroscopy (EDS) capability was used to study the phase distribution and composition. Gaseous phase hydrogen storage characteristics for each sample were measured using a Suzuki-Shokan multi-channel pressure-concentration-temperature (PCT, Suzuki Shokan, Tokyo, Japan) system. A piece of ingot was freshly cleaved before putting in the PCT ample holder. PCT sample was first hydrided and dehydrided at 30°C , followed by a 2 h, 400°C degassing with a vacuum pump. PCT isotherms at 90°C , 30°C , and 60°C were then measured with a 2 h, 400°C

degassing between measurements. Details of electrode preparations as well as measurement methods have been reported previously [17,18].

3. Results and Discussion

3.1. X-Ray Diffraction Structure Analysis

Eight alloys were prepared by arc melting, and their compositions were verified by ICP. XRD patterns of the alloys are shown in Figure 1. Three major peaks are detected in all alloys and belong to a BCC structure. Most of the peak intensity ratios are similar except for $I(200)/I(110)$ in Alloy-Nb (alloy with partial replacement of Nb). Among all substitutions, elemental Nb and Mo are similar in size and both have a BCC structure; however, only Alloy-Nb has the unusually larger (200) peak. The reason for such phenomenon is not clear and requires further structural refinement analysis. In addition to the main phase, one or more secondary phases can be found in the XRD pattern of each alloy apart from Alloy-Nb.

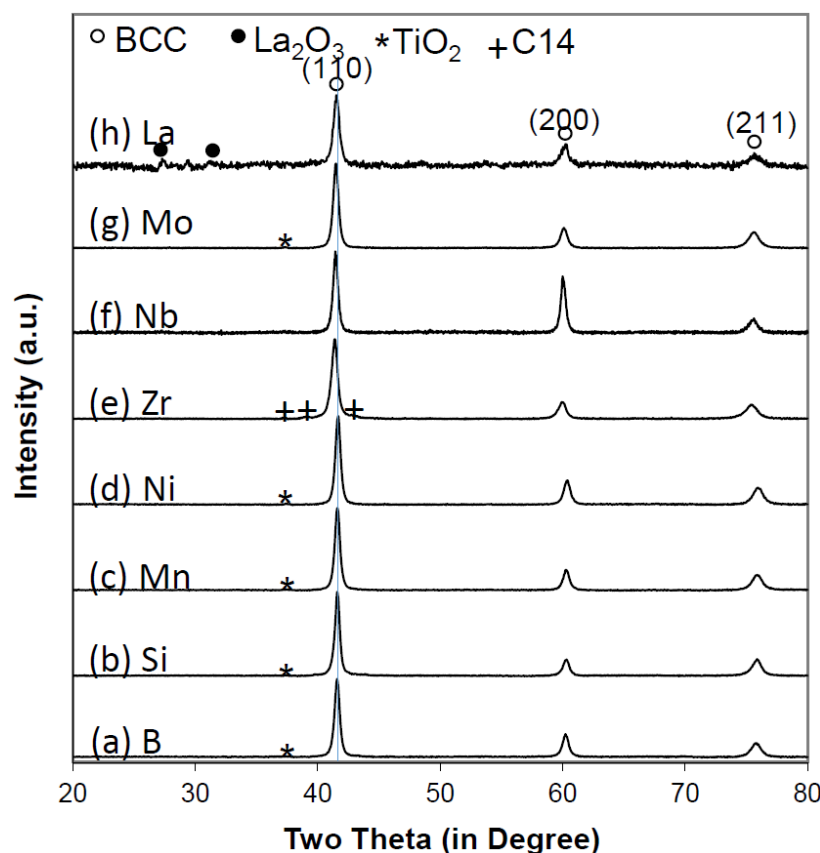


Figure 1. XRD patterns using Cu-K α as the radiation source for $Ti_{40}V_{30}Cr_{15}Mn_{13}X_2$ alloys, where $X = \text{(a)} B; \text{(b)} Si; \text{(c)} Mn; \text{(d)} Ni; \text{(e)} Zr; \text{(f)} Nb; \text{(g)} Mo$; and $\text{(h)} La$. The vertical line is used to indicate shifts in the body-centered-cubic (BCC) peak (110) with respect to that in $Ti_{40}V_{30}Cr_{15}Mn_{15}$ alloy.

Rietveld refinement results from the XRD analysis are summarized in Table 1. Lattice parameter a of the BCC phase ranges from 3.0679 Å to 3.0839 Å, which is larger than the optimized value of 3.042 Å corresponding to the maximized hydrogen storage capacity [19], leaving room for potential improvement in storage capacity for future studies.

Table 1. Summary of X-ray diffraction (XRD) results from alloys $Ti_{40}V_{30}Cr_{15}Mn_{13}X_2$.

X	<i>a</i> of BCC phase	BCC phase abundance	Secondary phase	<i>a</i> of secondary phase	<i>c</i> of secondary phase	Secondary phase abundance
	Å	wt%		Å	Å	wt%
B	3.0703	98.2	TiO ₂	4.1761	-	1.8
Si	3.0679	96.9	TiO ₂	4.1472	-	3.1
Mn	3.0687	98.9	TiO ₂	4.1687	-	1.1
Ni	3.0649	99.7	TiO ₂	4.1567	-	0.3
Zr	3.0839	98.2	C14	4.9895	8.1790	1.8
Nb	3.0790	99.8	TiO ₂	4.1743	-	0.2
Mo	3.0774	99.6	TiO ₂	4.1706	-	0.4
La	3.0693	98.3	La ₂ O ₃	11.302	-	1.7

The BCC lattice constant a is plotted against the atomic radius of the substituting element in Figure 2. Alloys substituted with transition metals show a linear relationship between the lattice constant and atomic radius (represented by the straight line in Figure 2). B and Si, with smaller atomic radii and larger electronegativity, do not shrink the BCC unit cell volume, which is possibly due to the electrons transferred from neighboring atoms and increases in the radius. Similar behavior has been found in the increase in the radius of B and Si in the Laves phase intermetallic compound [20]. La, with the largest atomic radius, does not change the BCC lattice constant, indicating La does not enter the BCC phase. According to the results of Rietveld refinement, the BCC phase abundances in all alloys are greater than 96.9%. TiO₂ is the dominating secondary phase, with some exceptions, seen in Alloy-Zr (C14), Alloy-Ni (TiNi observed in the SEM/EDS analysis as discussed in the next section), and Alloy-La (La₂O₃). Zr is known to promote the Laves phase in BCC-predominant alloys [21–26]. TiNi is a common phase seen in C14-predominant alloys with high concentration of Ni [27–30]. The main diffraction peak of TiNi overlaps with BCC (110) and, therefore, is indistinguishable in the XRD pattern (Figure 1). La₂O₃ was formed since La is too large to be included in the BCC phase, agreeing with the immiscibility shown in the La-V binary phase diagram [31].

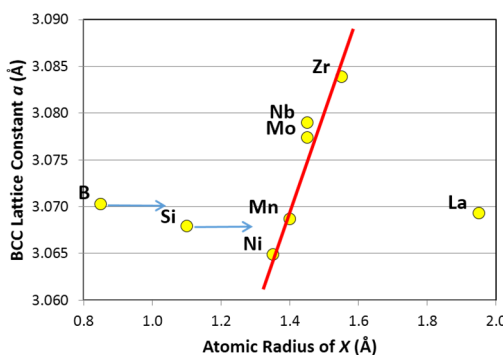


Figure 2. BCC lattice constant a vs. atomic radius of the partial substitution element X in $Ti_{40}V_{30}Cr_{15}Mn_{13}X_2$ alloys. There is a linear dependence when X is a transition metal. Addition of the largest La does not change the BCC lattice constant because La does not dissolve in the BCC phase and, instead, forms La₂O₃ secondary phase. Adding relatively small B and Si with higher electronegativity do not shrink the BCC unit cell because these atoms attract electrons from neighboring metallic atoms.

3.2. Scanning Electron Microscope/Energy Dispersive Spectroscopy Microstructure Analysis

Microstructures of the alloys were studied using SEM. The back-scattering electron images (BEI) are presented in Figure 3.

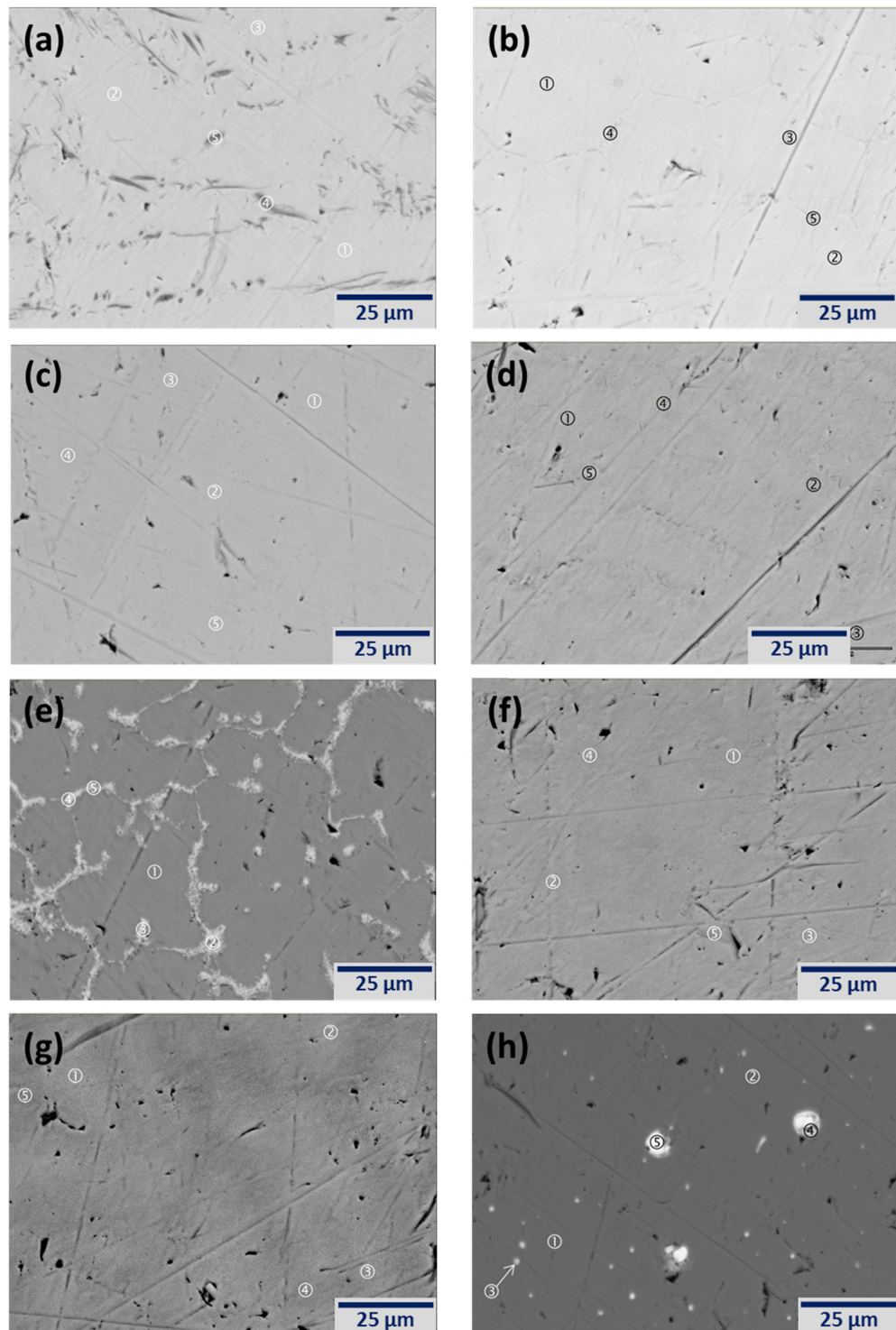


Figure 3. Scanning electron microscope (SEM) back-scattering electron images (BEI) for Ti₄₀V₃₀Cr₁₅Mn₁₃X₂ alloys, where X = (a) B; (b) Si; (c) Mn; (d) Ni; (e) Zr; (f) Nb; (g) Mo; and (h) La. Chemical compositions in the numbered areas measured by energy dispersive spectroscopy (EDS) are listed in Table 2.

EDS, although a semi-quantitative analysis, was used to study the chemical compositions of several spots with different contrasts identified numerically in the micrographs (Figure 3), and the results are summarized in Table 2 due to convenience and availability.

Table 2. Summary of energy dispersive spectroscopy (EDS) results. All compositions are in at%. Compositions of BCC phase are in **bold**.

Location	Ti	V	Cr	Mn	X	Phase
Figure 3a-1	41.1	29.3	16.7	12.9	0.0	BCC
Figure 3a-2	42.2	28.0	16.2	13.7	0.0	BCC
Figure 3a-3	42.2	28.2	16.3	13.3	0.0	BCC
Figure 3a-4	59.5	23.9	9.3	7.3	0.0	Oxide
Figure 3a-5	64.4	22.5	7.6	5.5	0.0	Oxide
Figure 3b-1	38.7	31.9	15.8	12.1	1.6	BCC
Figure 3b-2	38.4	32.2	15.8	12.1	1.5	BCC
Figure 3b-3	49.7	15.4	12.0	15.4	7.5	Oxide
Figure 3b-4	55.8	15.3	10.5	12.6	5.8	Oxide
Figure 3b-5	55.6	17.4	10.2	11.5	5.2	Oxide
Figure 3c-1	38.8	30.1	15.8	15.3	0.0	BCC
Figure 3c-2	38.7	29.9	15.9	15.5	0.0	BCC
Figure 3c-3	41.6	26.4	14.9	17.0	0.0	BCC
Figure 3c-4	43.3	26.2	14.6	15.9	0.0	BCC
Figure 3c-5	42.1	25.9	14.9	17.1	0.0	BCC
Figure 3d-1	36.9	33.8	16.6	11.4	1.3	BCC
Figure 3d-2	38.6	31.9	16.1	12.0	1.3	BCC
Figure 3d-3	42.6	28.2	14.7	12.4	2.1	BCC
Figure 3d-4	51.1	16.8	10.0	12.6	9.4	TiNi
Figure 3d-5	57.9	9.1	5.9	11.2	16.0	TiNi
Figure 3e-1	39.7	31.3	15.7	12.1	1.1	BCC
Figure 3e-2	43.1	19.9	13.3	15.9	7.7	C14/Zr _x Ni _y
Figure 3e-3	32.9	19.3	16.7	20.4	10.6	C14/Zr _x Ni _y
Figure 3e-4	31.5	17.9	16.4	21.5	12.7	C14/Zr _x Ni _y
Figure 3e-5	39.0	17.3	14.8	18.4	10.5	C14/Zr _x Ni _y
Figure 3f-1	38.7	32.8	15.1	11.3	2.1	BCC
Figure 3f-2	39.6	31.6	14.9	11.8	2.1	BCC
Figure 3f-3	39.6	31.8	14.9	11.6	2.1	BCC
Figure 3f-4	43.3	27.8	14.1	13.0	1.9	BCC
Figure 3f-5	45.1	25.9	13.9	13.3	1.9	BCC
Figure 3g-1	40.5	29.9	16.1	12.0	1.5	BCC
Figure 3g-2	41.4	29.0	16.1	12.3	1.3	BCC
Figure 3g-3	42.1	27.9	15.9	12.9	1.2	BCC
Figure 3g-4	44.9	25.5	15.3	13.6	0.7	BCC
Figure 3g-5	46.7	23.6	14.9	14.3	0.6	BCC
Figure 3h-1	45.5	26.1	13.9	14.5	0.0	BCC
Figure 3h-2	43.6	28.2	14.5	13.6	0.0	BCC
Figure 3h-3	34.0	24.2	10.5	9.1	22.2	La ₂ O ₃
Figure 3h-4	16.1	10.4	1.0	5.6	66.9	La ₂ O ₃
Figure 3h-5	5.0	2.9	1.0	0.0	91.2	La

Except for B and La, the substituting element is present in the BCC phase, ranging in content from 1.1 at% to 2.1 at%. EDS, although a semi-quantitative analysis, was used to study the chemical compositions of several spots with different contrasts identified numerically in the micrographs (Figure 3), and the results are summarized in Table 2 due to convenience and availability. Except for B and La, the substituting element is present in the BCC phase, ranging in content from 1.1 at% to 2.1 at%. The EDS system used for the current study cannot quantify the amount of lighter elements, such as B. According to the XRD and SEM-BEI analyses, the B-predominating phase does not exist; therefore, it is assumed that B is distributed in the BCC phase. Area with darker contrast in Alloy-B and Alloy-Si (Figure 3a-4,3a-5,3b-3,3b-4,3b-5) are small TiO_2 particles embedded in the BCC matrix. Alloy-Mn, Alloy-Nb, and Alloy-Mo are uniform in composition. In Alloy-Ni, the TiNi secondary phase was found (Figure 3d-4,3d-5). The $\text{C}14/\text{Zr}_x\text{Ni}_y$ phase in Alloy-Zr distributes inter-granularly since the BCC phase solidifies first and pushes Zr into the $\text{C}14$ phase. Average electron density (e/a) of the secondary phase in Alloy-Zr is 5.06, which is below the $\text{C}14/\text{C}15$ threshold [32,33] and is, therefore, another piece of evidence that the secondary phase is $\text{C}14$ rather than $\text{C}15$ in addition to the findings in XRD analysis. B/A in this $\text{C}14$ phase is in the range of 0.97 to 1.3, which is way too low for an AB_2 with a perfect B/A of 2.0. Since there is no major shift in XRD peaks of $\text{C}14$, these areas are not hypo-stoichiometric AB_2 . Therefore, other Zr_xNi_y secondary phase must also co-exist in this $\text{C}14$ phase, as in the case of AB_2 -predominated alloys [34,35]. Since the B/A ratios of the components of Zr_xNi_y ($\text{Zr}_7\text{Ni}_{10}$, $\text{Zr}_9\text{Ni}_{11}$, TiNi , and ZrNi) are all below 2.0, their existence will lower the B/A ratio in this region. In Alloy-La, La does not precipitate in the main BCC phase. La either forms a large metallic inclusion (Figure 3h-5) or an oxide suspended uniformly in the BCC matrix (Figure 3h-3)/near the edge of La metallic clusters (Figure 3h-4). The zero-solubility of La in BCC explains why the addition of La does not change the BCC lattice constant (Figure 2).

3.3. Gaseous Phase Study

PCT analysis was used to characterize the gaseous phase hydrogen storage properties of alloys in this study. The chamber containing the sample was filled with 7 MPa of hydrogen at 30 °C, and then the absorption amount was calculated, followed by a PCT desorption measurement at the same temperature. The sample was degassed at 400 °C for 2 h with a mechanical vacuum pump, and then a full 60 °C absorption-desorption PCT was measured. The sample was degassed at 400 °C for 2 h again, followed by a 90 °C PCT measurement. Finally, it was degassed at 400 °C for 2 h, and a last 30 °C PCT measurement was conducted. Absorption and desorption isotherms measured at 30 °C, 60 °C, and 90 °C together with the initial 30 °C desorption isotherm are shown in Figure 4. Information obtained from the PCT study is summarized in Table 3. Most of the alloys show similar gaseous phase properties. Except for Alloy-Zr (3.12 wt%), the pristine alloys have similar maximum storage capacities in the range of 3.30 wt% to 3.55 wt%. A storage capacity of 3.50 wt% can be translated into an electrochemical discharge capacity $938 \text{ mAh}\cdot\text{g}^{-1}$ based on 1 wt% of hydrogen storage is equivalent to $268 \text{ mAh}\cdot\text{g}^{-1}$. Maximum storage capacities measured at 30 °C and 60 °C after 400 °C degassing show the following trend: substitution of B > Mo ~ Nb ~ La > Ni ~ Mn ~ Si > Zr, which demonstrate very weak correlations to the BCC unit cell volume (correlation factors $R^2 = 0.18$ and 0.22 for storage capacities at 30 °C and 60 °C, respectively, indicating larger BCC unit cell corresponds to lower capacity) that were opposite to

was expected. In general, reversibility of these alloys (ratio of revisable capacity down to 0.001 MPa and maximum capacity) is much worse than that of AB₂ or AB₅ MH alloy because of the fact the first pressure plateau between BCC and body-center-tetragonal (BCT) phases is too low to be observed with our PCT apparatus. While Alloy-B shows the best reversibility at 30 °C, Alloy-Mn and Alloy-Ni have better reversibility at 60 °C than others. Average reversible 30 °C storage capacity is about 0.7 wt%, which is equivalent to an electrochemical discharge capacity of 188 mAh·g⁻¹. The 90 °C desorption plateau pressure of Alloy-Ni is much higher than those of other alloys. Hysteresis of the PCT isotherm is defined as $\ln(P_a/P_d)$, where P_a and P_d are the absorption and desorption equilibrium pressures at 2.0 wt% hydrogen storage, respectively. In this series of alloys, only PCT hysteresis at 90 °C can be measured. All substitutions show similar or slightly lower hysteresis, except for Si. PCT hysteresis is mainly from the energy required to elastically deform the lattice near the metal/MH interface during hydrogenation. Most substitutions increase the chemical disorder and reduce the PCT hysteresis. Nb has the same BCC crystal structure as Mn, therefore its effects on the degree of disorder and PCT hysteresis are limited. Adding Si with covalent bonding may stiffen the lattice, requiring higher energy to expand the MH phase in the host metal.

Due to the low desorption plateau pressure in these alloys, the regular thermodynamic calculation cannot be performed. Instead, the absorption equilibrium pressures at 2.0 wt% hydrogen storage at 60 °C and 90 °C were used to estimate the changes in enthalpy (ΔH) and entropy (ΔS) by the equation:

$$\Delta G = \Delta H - T\Delta S = RT\ln P \quad (1)$$

where R is the ideal gas constant and T is the absolute temperature. Results of these calculations are listed in Table 3. Compared to the base Alloy-Mn, all substitutions decrease ΔH except for Zr, which indicates that Zr decreases the hydride stability. In the case of Alloy-Zr, addition of the C14 phase in the alloy facilitates hydrogen absorption through the synergetic effect between the storage and catalytic phases [36] and destabilizes the hydride. ΔS , usually calculated with the desorption isotherm, is an indication of how far the MH system is from a perfect and ordered situation. The theoretical value of ΔS is the entropy of hydrogen gas, which is close to $-130 \text{ J}\cdot\text{mol}^{-1}\cdot\text{K}^{-1}$ [37]. In our calculation, all substitutions decrease ΔS to below $-135 \text{ J}\cdot\text{mol}^{-1}\cdot\text{K}^{-1}$ except for Zr, which is an indication that a more ordered MH system was formed. Alloy-Zr shows a relatively high value of ΔS , suggesting a more disordered MH system was formed, possibly due to the interaction between the main BCC and C14 secondary phases.

One interesting feature in the PCT isotherms caught one of the authors' (Ouchi) attention: several alloys—Alloy-B, Alloy-Zr, Alloy-Nb, and Alloy-Mo—show a small plateau near 0.3 MPa on the 30 °C desorption curve while others do not. This plateau, although very small (about 0.10 wt% to 0.16 wt%), is at a pressure just above one atmosphere (0.1 MPa) and can be from a catalytic phase that has not been reported previously. The importance of this phase with respect to electrochemical performance will be discussed in the discussion section of this paper.

Table 3. Summary of gaseous phase hydrogen storage properties. PCT: pressure-concentration-temperature.

X	Initial	30 °C	30 °C	60 °C	60 °C	90 °C desorption	90 °C hysteresis @2.0 wt% kJ·mol ⁻¹	-ΔH @2.0 wt% kJ·mol ⁻¹	-ΔS J·mol ⁻¹ ·K ⁻¹	PCT
	maximum capacity	maximum capacity	reversible capacity	maximum capacity	reversible capacity	pressure @2.0 wt%				plateau
	wt%	wt%	wt%	wt%	wt%	MPa				@0.3 MPa
B	3.48	3.38	1.73	3.43	1.00	0.011	1.7	67	181	Yes
Si	3.30	3.08	0.52	3.08	1.12	0.011	2.5	56	156	No
Mn	3.47	3.11	0.49	3.02	1.40	0.013	2.0	37	107	No
Ni	3.39	3.16	0.63	3.16	1.56	0.028	1.8	58	165	No
Zr	3.12	2.76	0.53	2.59	1.09	0.016	1.9	22	63	Yes
Nb	3.48	3.25	0.59	3.19	0.86	0.011	2.0	64	176	Yes
Mo	3.42	3.24	0.56	3.29	1.00	0.012	1.8	66	178	Yes
La	3.55	3.19	0.49	3.19	0.74	0.009	1.6	67	178	No

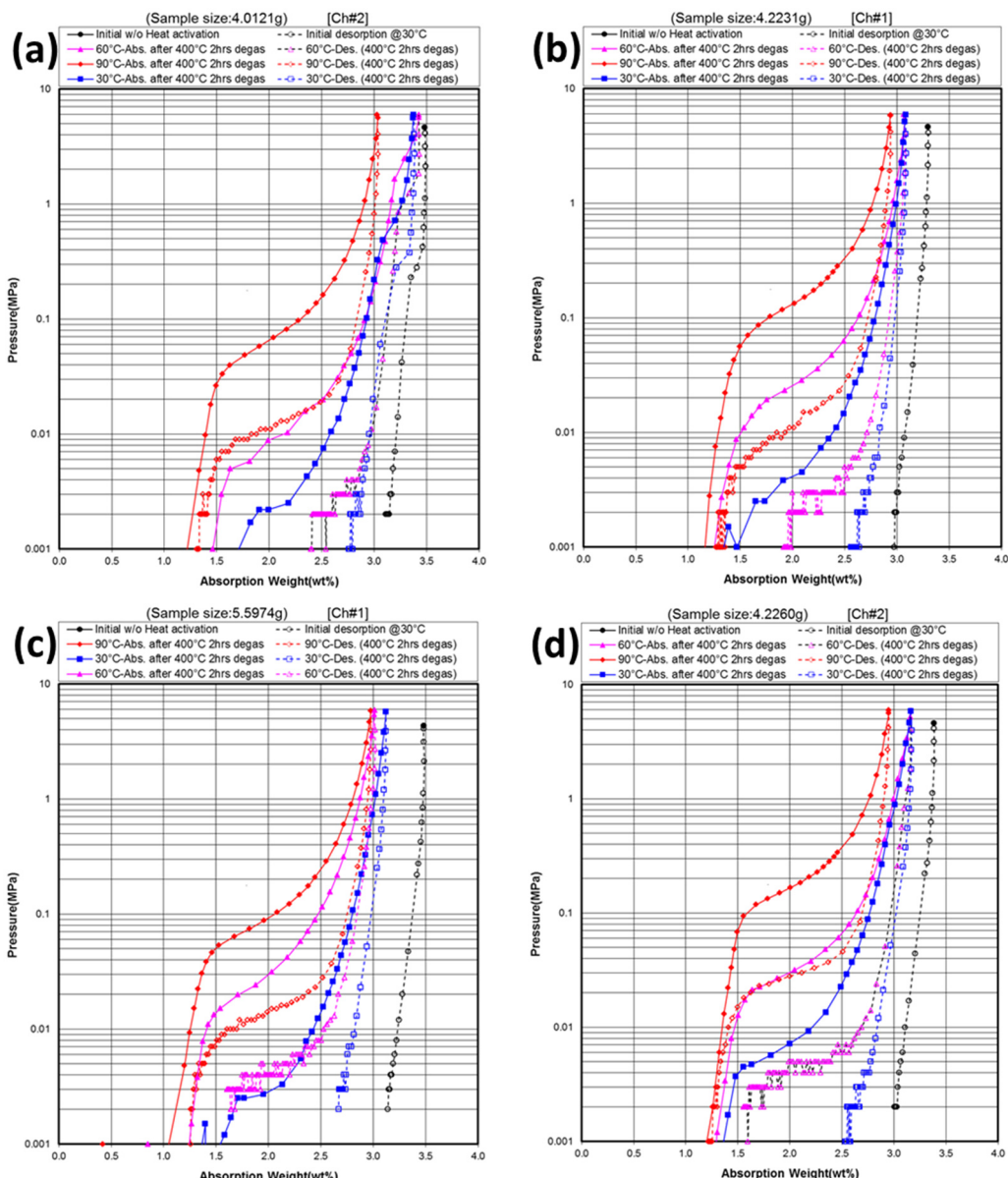


Figure 4. Cont.

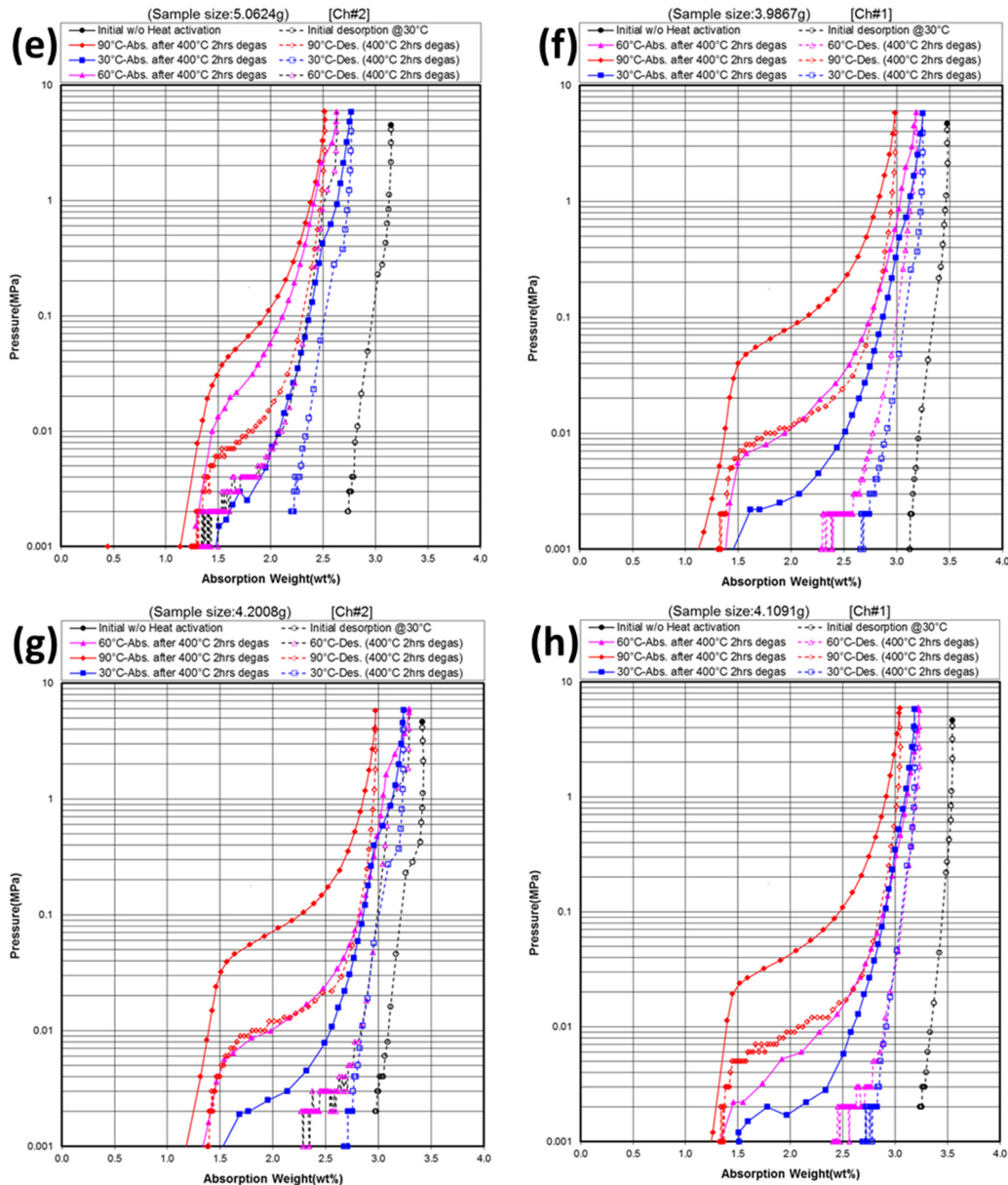


Figure 4. PCT isotherms measured at 30 °C (both before and after 400 °C degassing), 60 °C, and 90 °C for Ti₄₀V₃₀Cr₁₅Mn₁₃X₂ alloys, where X = (a) B; (b) Si; (c) Mn; (d) Ni; (e) Zr; (f) Nb; (g) Mo; and (h) La. Open and solid symbols are for absorption and desorption curves, respectively.

3.4. Electrochemical Measurement in 30% KOH

In a flooded half-cell, the electrochemical properties of MH alloys in this study were studied. Electrodes were made with powder after the PCT measurement and degassed four times at 400 °C for 2 h. No alkaline pretreatment was applied before the half-cell measurement. The charge condition was 10 h with a current density of 50 mA·g⁻¹ and discharged at the same rate initially and followed by two pulls at 12 mA·g⁻¹ and 4 mA·g⁻¹ with a cut-off voltage at 0.9 V *versus* the counter electrode. The 500 mAh total charge input was based on the maximum reversible gaseous phase capacity being 1.73% (429 mAh·g⁻¹). The charge and discharge voltage curves for Alloy-Mo are shown in Figure 5. The high resistance through the poor-conducting TiO₂ surface resulted from the highly-corrosive 30% KOH electrolyte may cause the large charge and discharge overpotentials [5].

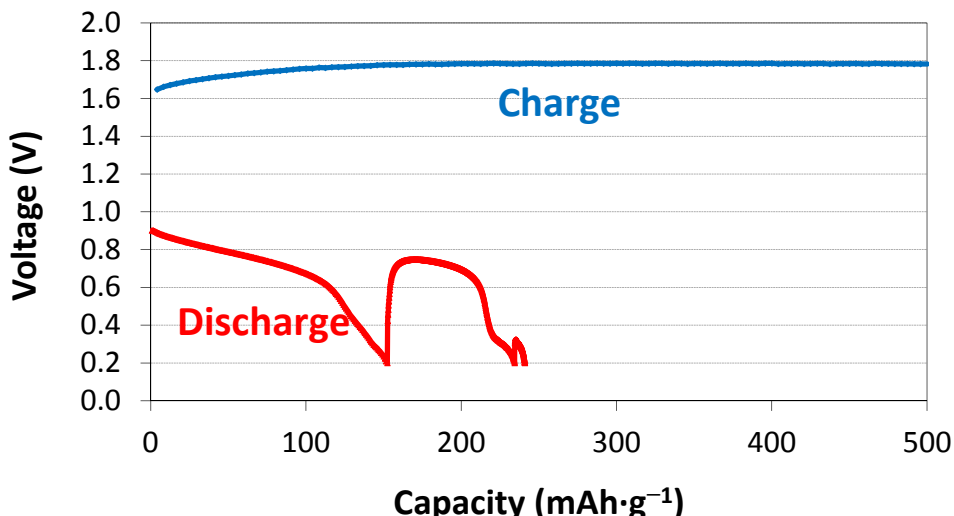


Figure 5. The first cycle charge and discharge voltage profiles for $\text{Ti}_{40}\text{V}_{30}\text{Cr}_{15}\text{Mn}_{13}\text{Mo}_2$.

Capacities totaled at 50, 12, and 4 $\text{mA}\cdot\text{g}^{-1}$ are listed in Table 4.

Table 4. Summary of electrochemical hydrogen storage properties.

X	1st cycle capacity @ 50 $\text{mA}\cdot\text{g}^{-1}$	1st cycle capacity @ 12 $\text{mA}\cdot\text{g}^{-1}$	1st cycle capacity @ 4 $\text{mA}\cdot\text{g}^{-1}$
	$\text{mAh}\cdot\text{g}^{-1}$	$\text{mAh}\cdot\text{g}^{-1}$	$\text{mAh}\cdot\text{g}^{-1}$
B	81	163	179
Si	8	14	16
Mn	12	20	24
Ni	33	47	61
Zr	64	130	144
Nb	41	68	79
Mo	152	234	247
La	23	39	41

About 50% of the capacity was obtained at the highest rate. The total capacity (totaled at 4 $\text{mA}\cdot\text{g}^{-1}$) for the first six cycles of each alloy is plotted in Figure 6a. All substitutions for Mn, except for Si, show improvement in the first cycle capacity. The first cycle capacity demonstrates the trend of substitution of Mo > B > Zr > Nb > Ni > La > Mn > Si. Alloy-Si has the highest hysteresis, indicating its proneness to pulverization [38] and, thus, poor electrochemical performance. Alloy-Mo shows the highest discharge capacity at 247 $\text{mAh}\cdot\text{g}^{-1}$. Partial Mo substitution in Ti-Cr MH alloy was reported previously, and it stabilized the BCC structure and improved the gaseous phase properties [39]. As seen in Figure 6a, capacity drops to almost nothing at the second cycle due mainly to the highly corrosive nature of 30% KOH electrolyte. The large amount of over-charge may also contribute to the severe capacity degradation. The original capacity of Alloy-Mo without corrosion from KOH can be extrapolated and is about double that obtained from the first cycle; in other words, electrochemical capacity close to 500 $\text{mAh}\cdot\text{g}^{-1}$ is possible if corrosion and passivation can be prevented from the use of non-corrosive electrolyte. In cycles two to six, Alloy-Ni with the TiNi phase shows the highest discharge capacity since the TiNi phase protects some portions of the bulk from being completely corroded. TiNi was found to increase the cycle stability of Laves phase MH alloys in a previous study [32].

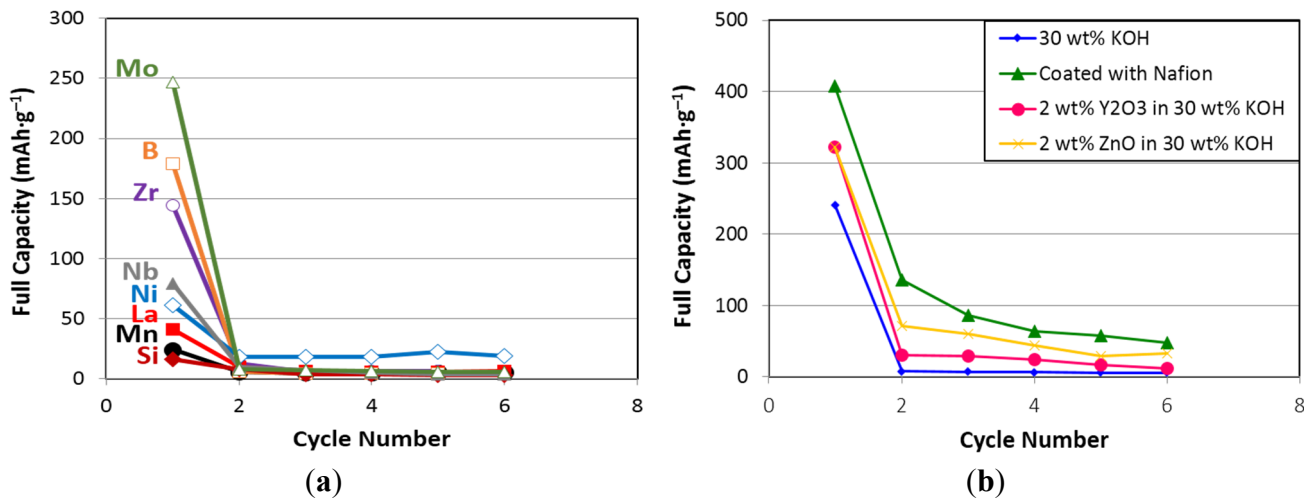


Figure 6. (a) Discharge capacities measured at $4 \text{ mA} \cdot \text{g}^{-1}$ in 30% KOH for $\text{Ti}_{40}\text{V}_{30}\text{Cr}_{15}\text{Mn}_{13}X_2$ alloys and (b) discharge capacities measured at $4 \text{ mA} \cdot \text{g}^{-1}$ for $\text{Ti}_{40}\text{V}_{30}\text{Cr}_{15}\text{Mn}_{13}\text{Mo}_2$ in modified electrolytes and with Nafion treatment.

A SEM micrograph taken from the surface of Alloy-Mo after six electrochemical cycles reveals severe pulverization (Figure 7a), and the EDS spectrum taken from the surface shows no trace of oxide (Figure 7b). It may be too thin and compact to be detected in the current study, but surface TiO_2 formed after cycling was reported previously in a BCC alloy [5] and can hinder the surface electrochemical reaction completely.

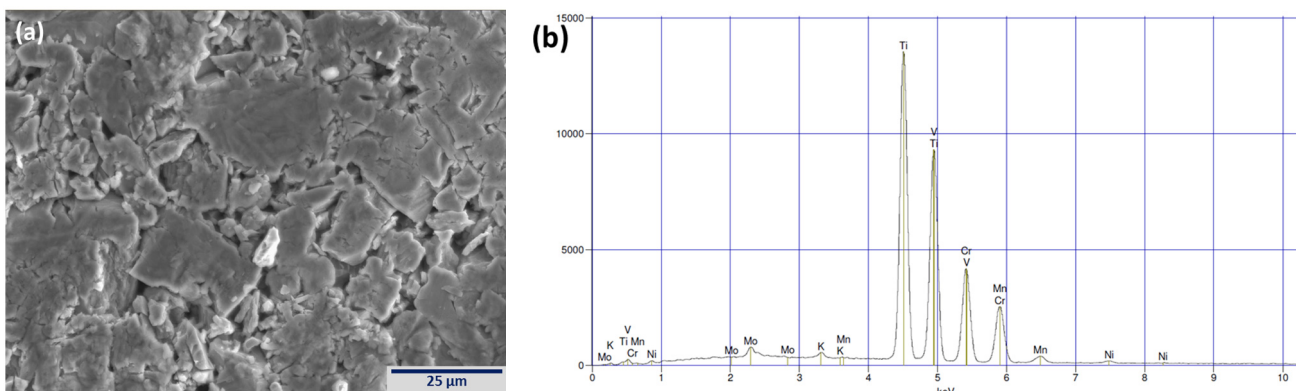


Figure 7. (a) SEM surface micrograph exhibiting the severe pulverization and (b) EDS spectrum showing negligible amount of oxygen on the surface after six electrochemical cycles with $\text{Ti}_{40}\text{V}_{30}\text{Cr}_{15}\text{Mn}_{13}\text{Mo}_2$.

In order to improve the cycle stability, preferential leaching, and surface passivation issues need to be addressed. Therefore, the effects of Y_2O_3 and ZnO additions in electrolyte and Nafion surface coating on electrode are investigated. It was found that by mixing Y_2O_3 powder to AB_5 alloy powder, dissolution of the alloy's constituent elements and formation of rare earth hydroxides were suppressed by an yttrium protective film on the alloy surface [40,41]. A small amount of Y_2O_3 dissolved in the alkaline electrolyte, and the yttrium complex ions were then adsorbed on or chemically bound to the surface of the alloy powder. ZnO , an amphoteric species, is nearly insoluble in water but soluble in acid and base. ZnO 's effect as an electrolyte additive on electrochemical degradation performance will be interesting to observe.

One drawback of Y_2O_3 addition is that the yttrium protective layer lowers the catalytic activity of the alloy surface and, consequently, reduces the surface charge transfer reaction [40]. In order to possibly solve such an issue, Nafion, which is hydrogen-permeable with great chemical stability, was also adopted in the current study. Nafion applied as a protective coating increased the first cycle capacity by up to 75% in an MgNi-based alloy [42]. For the electrolyte modification study, two electrolytes were made by adding 2 wt% Y_2O_3 and 2 wt% ZnO (both based on the amount of KOH) into 30% KOH and used in the half-cell measurements with Alloy-Mo. For the surface modification study, Alloy-Mo electrode was coated with Nafion (perfluorosulfonic acid-PTFT copolymer, 5 wt% in water and 1-propanol) by dipping it for 2 min in ethanol diluted Nafion solution, where the ethanol to Nafion solution ratio was 5:1 by weight, and then heat treating for 2 h at 120 °C under argon atmosphere. The total capacity of each treatment compared to that of standard 30% KOH is plotted in Figure 6b. The first cycle capacity is improved with the additions of Y_2O_3 and ZnO from 247 $\text{mAh}\cdot\text{g}^{-1}$ to 320 $\text{mAh}\cdot\text{g}^{-1}$, but it still drops dramatically at the second cycle due to pulverization. The additives were incorporated differently than they were the previous study, where pasted electrode was made using the mixture of additive, alloy powder, and water [40]. The wet method can perhaps provide a better distribution of additive and more complete protection for the alloy. Among all treatments, Nafion coating on electrode is the most effective in improving the first cycle capacity and achieves 408 $\text{mAh}\cdot\text{g}^{-1}$, but degradation after the first cycle is still severe. After cycling, alloy particle pulverization (as seen from the SEM micrograph in Figure 7a) creates new surfaces that are not protected by the Nafion coating. Combination of surface coating (original robust protection) and electrolyte modification (continuous protection throughout cycling) may be advantageous for further corrosion and passivation inhibitions.

3.5. Discussion

To further study the correlations between electrochemical discharge capacity and various properties, correlation factors R^2 from linear regression are calculated and listed in Table 5. All correlations with gaseous phase properties are insignificant.

Table 5. Correlation factor (R^2) between electrochemical discharge capacity and various gaseous phase hydrogen storage properties. A R^2 value closer to one indicates better linear correlation between the two variables.

Correlation factor	Initial maximum capacity	30 °C maximum capacity	30 °C reversible capacity	60 °C maximum capacity	60 °C reversible capacity	90 °C desorption pressure @2 wt%	90 °C hysteresis @2 wt%	BCC lattice constant a	Plateau width
$R^2 =$	0.02	0.03	0.17	0.04	0.06	0.01	0.19	0.02	0.29

Correlation with BCC lattice constant is only marginally significant ($R^2 = 0.29$) and plotted in Figure 8a, showing the enlargement of unit cell results in an increase in electrochemical capacity but not in a strictly linear relationship.

One significant correlation can be established between electrochemical capacity and occurrence of a small plateau near 0.3 MPa on the 30 °C desorption isotherm. Among all alloys, Alloy-B, Alloy-Zr, Alloy-Nb, and Alloy-Mo have this plateau at around 0.3 MPa and also the highest electrochemical discharge capacity. This plateau is from an intermediate hydride phase that can be catalytic and improve

the electrochemical reaction. Electrochemical discharge capacity is plotted against width of the plateau at around 0.3 MPa (0.16 wt% for Alloy-B, 0.09 wt% for Alloy-Zr, 0.08 wt% Alloy-Nb, and 0.10 wt% for Alloy-Mo, which is defined as the width of concentration difference between the extrapolations from two neighboring isotherms) in Figure 8b and shows a strong correlation with $R^2 = 0.70$. Furthermore, correlation with transition metal substitution is even stronger as seen from the straight line connecting points from Alloy-Mo, Alloy-Zr, and Alloy-Nb. Electrochemical discharge capacity is mainly dominated by the catalytic phase formed during hydrogenation.

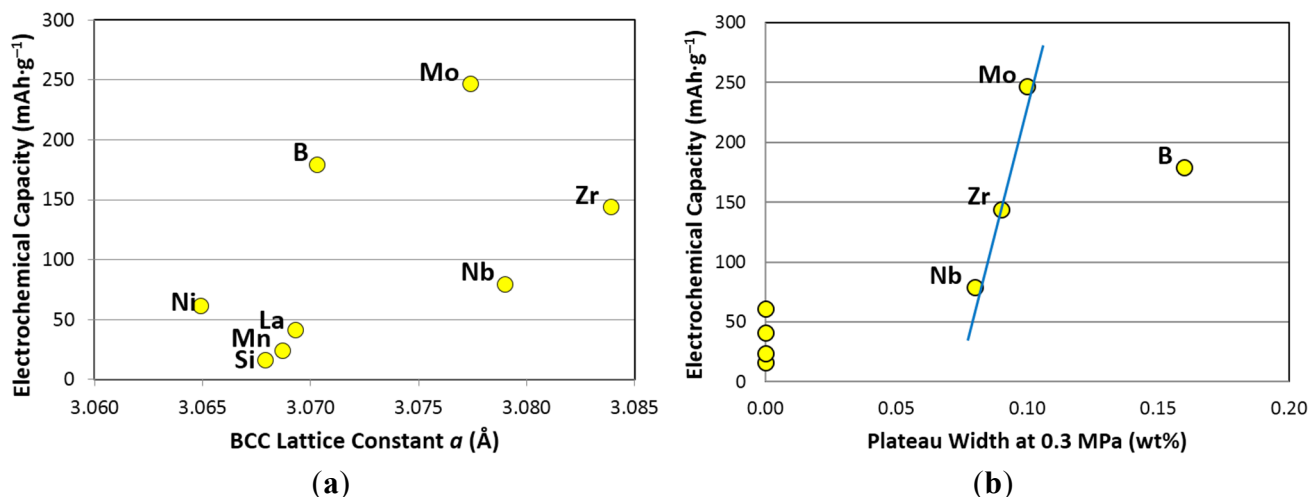


Figure 8. (a) Discharge capacities measured at $4 \text{ mA}\cdot\text{g}^{-1}$ vs. BCC lattice constant and (b) vs. width of 0.3 MPa pressure plateau. The straight line in Figure 8b is to illustrate the linear correlation between capacity and plateau width at 0.3 MPa of the transition metal substitution.

4. Conclusions

Various hydrogen storage properties in gaseous phase and in electrochemistry of a series of TiVCrMn-based BCC alloys with different partial substitutions for Mn with B, Si, Ni, Zr, Nb, Mo, and La were investigated. All substitutions went into the BCC phase except for La. While Ni promoted the formation of TiNi secondary phase that provided better cycle stability, Zr promoted the formation of C14 secondary phase, which did not affect any of the properties significantly due to its small abundance. Correlations between gaseous phase properties and lattice constant were not clear.

A newly discovered catalytic phase formed during hydrogenation was found to be very critical for the electrochemical discharge capacity performance. This phase enabled the electrochemical application of BCC-only alloys without contributions from secondary phases. The highest discharge capacity of $247 \text{ mAh}\cdot\text{g}^{-1}$ was obtained from $\text{Ti}_{40}\text{V}_{30}\text{Cr}_{15}\text{Mn}_{13}\text{Mo}_2$ alloy with both a catalytic hydride phase at around 0.3 MPa and an enlarged BCC unit cell. Further improvement in electrochemical capacity of this alloy reached as high as $408 \text{ mAh}\cdot\text{g}^{-1}$ when a protective Nafion coating was applied on the electrode. Substitutions of B, Nb, and Zr also improved the electrochemical capacity but at a lesser degree.

Acknowledgments

This work is financially supported by Advanced Research Projects Agency-Energy (ARPA-E) under the robust affordable next generation EV-storage (RANGE) program (DE-AR0000386).

Conflicts of Interest

The authors declare no conflict of interest.

References

- Young, K.; Fetcenko, M.A.; Ouchi, T.; Im, J.; Ovshinsky, S.R.; Li, F.; Reinhout, M. Hydrogen Storage Materials Having Excellent Kinetics, Capacity, and Cycle Stability. U.S. Patent 7,344,676, 18 March 2008.
- Lee, H.; Chourashiya, M.G.; Park, C.; Park, C. Hydrogen storage and electrochemical properties of the $Ti_{0.32}Cr_{0.43-x-y}V_{0.25}Fe_xMn_y$ ($x = 0\text{--}0.055$, $y = 0\text{--}0.080$) alloys and their composites with $MmNi_{3.99}Al_{0.29}Mn_{0.3}Co_{0.6}$ alloy. *J. Alloys Compd.* **2013**, *566*, 37–42.
- Inoue, H.; Arai, S.; Iwakura, C. Crystallographic and electrochemical characterization of $TiV_{4-x}Ni_x$ alloys for nickel-metal hydride batteries. *Electrochim. Acta* **1996**, *41*, 937–939.
- Mori, T.; Iba, H. Hydrogen-absorbing Alloy and Hydrogen-absorbing Alloy Electrode. U.S. Patent 6,338,764, 15 January 2002.
- Yu, X.B.; Wu, Z.; Xia, B.J.; Xu, N.X. A Ti-V-based bcc phase alloy for use as metal hydride electrode with high discharge capacity. *J. Chem. Phys.* **2004**, *121*, 987–990.
- Chen, N.; Li, R.; Zhu, Y.; Liu, Y.; Pan, H. Electrochemical hydrogenation and dehydrogenation mechanisms of the Ti-V base multiphase hydrogen storage electrode alloy. *Acta Metal. Sin.* **2004**, *40*, 1200–1204.
- Iba, H.; Akiba, E. The relation between microstructure and hydrogen absorbing property in Laves phase-solid solution multiphase alloys. *J. Alloys Compd.* **1995**, *231*, 508–512.
- Rönnebro, E.; Noréus, D.; Sakai, T.; Tsukahara, M. Structural studies of a new Laves phase alloy $(Hf,Ti)(Ni,V)_2$ and its very stable hydride. *J. Alloys Compd.* **1995**, *231*, 90–94.
- Tsukahara, M.; Takahashi, K.; Mishima, T.; Isomura, A.; Sakai, T. V-based solid solution alloys with Laves phase network: Hydrogen absorption properties and microstructure. *J. Alloys Compd.* **1996**, *236*, 151–155.
- Qiu, S.; Chu, H.; Zhang, Y.; Sun, D.; Song, X.; Sun, L.; Xu, F. Electrochemical kinetics and its temperature dependence behaviors of $Ti_{0.17}Zr_{0.08}V_{0.35}Cr_{0.10}Ni_{0.30}$ alloy electrode. *J. Alloys Compd.* **2009**, *471*, 453–456.
- Young, K.; Nei, J.; Wong, D.F.; Wang, L. Structural, hydrogen storage, and electrochemical properties of Laves phase-related body-centered-cubic solid solution metal hydride alloys. *Int. J. Hydrog. Energy* **2014**, *39*, 21489–21499.
- Young, K.; Wong, D.F.; Wang, L. Effect of Ti/Cr content on the microstructures and hydrogen storage properties of Laves phase-related body-centered-cubic solid solution alloys. *J. Alloys Compd.* **2015**, *622*, 885–893.
- Young, K.; Ouchi, T.; Nei, J.; Meng, T. Effects of Cr, Zr, V, Mn, Fe, and Co to the hydride properties of Laves phase-related body-centered-cubic solid solution alloys. *J. Power Sources* **2015**, *281*, 164–172.
- Yan, Y.; Chen, Y.; Liang, H.; Zhou, X.; Wu, C.; Tao, M.; Pang, L. Hydrogen storage properties of V–Ti–Cr–Fe alloys. *J. Alloys Compd.* **2008**, *454*, 427–431.

15. Huot, J.; Akiba, E.; Ogura, T.; Ishido, Y. Crystal structure, phase abundance and electrode performance of Laves phase compounds (Zr, A) V_{0.5}Ni_{1.1}Mn_{0.2}Fe_{0.2} (A = Ti, Nb or Hf). *J. Alloys Compd.* **1995**, *218*, 101–109.
16. Iba, H.; Akiba, E. Hydrogen absorption and modulated structure in Ti–V–Mn alloys. *J. Alloys Compd.* **1997**, *253–254*, 21–24.
17. Young, K.; Fetcenko, M.A.; Li, F.; Ouchi, T. Structural, thermodynamic, and electrochemical properties of Ti_xZr_{1-x}(VNiCrMnCoAl)₂ C14 Laves phase alloys. *J. Alloys Compd.* **2008**, *464*, 238–247.
18. Young, K.; Fetcenko, M.A.; Koch, J.; Morii, K.; Shimizu, T. Studies of Sn, Co, Al, and Fe additives in C14/C15 Laves alloys for NiMH battery application by orthogonal arrays. *J. Alloys Compd.* **2009**, *486*, 559–569.
19. Yoshida, M.; Akiba, E. Hydrogen absorbing-desorbing properties and crystal structure of the Zr–Ti–Ni–Mn–V AB₂ Laves phase alloys. *J. Alloys Compd.* **1995**, *224*, 121–126.
20. Gakkai, N.K. *Hi Kagaku Ryouron teki Kinzoku Kagobutu*; Maruzen: Tokyo, Japan, 1975; p. 296. (In Japanese)
21. Huot, H.; Akiba, E.; Ishido, Y. Crystal structure of multiphase alloys (Zr,Ti)(Mn,V)₂. *J. Alloys Compd.* **1995**, *231*, 85–89.
22. Kuriwa, T.; Tamura, T.; Amemiya, T.; Fuda, T.; Kamegawa, A.; Takamura, H.; Okada, M. New V-based alloys with high protium absorption and desorption capacity. *J. Alloys Compd.* **1999**, *293–295*, 433–436.
23. Young, K.; Ouchi, T.; Fetcenko, M.A. Roles of Ni, Cr, Mn, Sn, Co, and Al in C14 Laves phase alloys for NiMH battery application. *J. Alloys Compd.* **2009**, *476*, 774–781.
24. Bendersky, L.A.; Wang, K.; Levin, I.; Newbury, D.; Young, K.; Chao, B.; Creuziger, A. Ti_{12.5}Zr₂₁V₁₀Cr_{8.5}Mn_xCo_{1.5}Ni_{46.5-x} AB₂-type metal hydride alloys for electrochemical storage application: Part 1. Structural characteristics. *J. Power Sources* **2012**, *218*, 474–486.
25. Young, K.; Ouchi, T.; Huang, B.; Reichman, B.; Blankenship, R. Improvement in –40 °C electrochemical properties of AB₂ metal hydride alloy by silicon incorporation. *J. Alloys Compd.* **2013**, *575*, 65–72.
26. Young, K.; Reichman, B.; Fetcenko, M.A. Electrochemical performance of AB₂ metal hydride alloys measured at –40 °C. *J. Alloys Compd.* **2013**, *580*, S349–S352.
27. Smith, J.F.; Lee, K.J. La-V (Lanthanum-Vanadium). In *Binary Alloy Phase Diagram*, 2nd ed.; Massalski, T.B., Okamoto, H., Subramanian, P.R., Kacprzak, L., Eds.; ASM International: Geauga County, OH, USA, 1990; Volume 3, pp. 2437–2439.
28. Nei, J.; Young, K.; Salley, S.O.; Ng, K.Y.S. Determination of C14/C15 phase abundance in Laves phase alloys. *Mater. Chem. Phys.* **2012**, *136*, 520–527.
29. Nei, J.; Young, K.; Regmi, R.; Lawes, G.; Salley, S.O.; Ng, K.Y.S. Gaseous phase hydrogen storage and electrochemical properties of Zr₈Ni₂₁, Zr₇Ni₁₀, Zr₉Ni₁₁, and ZrNi metal hydride alloys. *Int. J. Hydrog. Energy* **2012**, *37*, 16042–16055.
30. Züttle, A. Materials for hydrogen storage. *Mater. Today* **2003**, *6*, 24–33.
31. Huang, T.; Li, J.; Yu, J.; Liu, Z.; Mao, S.; Zhang, Y.; Sun, G.; Han, J.; Ren, H.; Chen, J. Influence of partial substitution of Mo for Cr on structure and hydrogen storage characteristics of non-stoichiometric Laves phase TiCrB_{0.9} alloy. *Int. J. Hydrog. Energy* **2013**, *38*, 11955–11963.

32. Young, K.; Nei, J.; Ouchi, T.; Fetcenko, M.A. Phase abundances in AB₂ metal hydride alloys and their correlations to various properties. *J. Alloys Compd.* **2011**, *509*, 2277–2284.
33. Johnston, R.L.; Hoffmann, R. Structure-bonding relationships in the Laves phases. *Z. Anorg. Allg. Chem.* **1992**, *616*, 105–120.
34. Boettinger, W.J.; Newbury, D.E.; Wang, K.; Bendersky, L.A.; Chiu, C.; Kattner, U.R.; Young, K.; Chao, B. Examination of multiphase (Zr,Ti)(V,Cr,Mn,Ni)₂ Ni-MH electrode alloys: Part I. Dendritic solidification structure. *Metall. Mater. Trans. A* **2010**, *41*, 2033–2047.
35. Bendersky, L.A.; Wang, K.; Boettinger, W.J.; Newbury, D.E.; Young, K.; Chao, B. Examination of multiphase (Zr,Ti)(V,Cr,Mn,Ni)₂ Ni-MH electrode alloys: Part II. Solid-state transformation of the interdendritic B₂ phase. *Metall. Mater. Trans. A* **2010**, *41*, 1891–1906.
36. Wong, D.F.; Young, K.; Nei, J.; Wang, L.; Ng, K.Y.S. Effects of Nd-addition on the structural, hydrogen storage, and electrochemical properties of C14 metal hydride alloys. *J. Alloys Compd.* **2015**, *647*, 507–518.
37. Lide, D.R. *CRC Handbook of Chemistry and Physics*, 74th ed.; CRC Press: Boca Raton, FL, USA, 1993; pp. 6–22.
38. Young, K.; Ouchi, T.; Fetcenko, M.A. Pressure-composition-temperature hysteresis in C14 Laves phase alloys: Part 1. Simple ternary alloys. *J. Alloys Compd.* **2009**, *480*, 428–433.
39. Kamegawa, A.; Shirasaki, K.; Tamura, T.; Kuriwa, T.; Takamura, H.; Okada, M. Crystal structure and protium absorption properties of Ti-Cr-X alloys. *Mater. Trans.* **2002**, *43*, 470–473.
40. Kaiya, H.; Ookawa, T. Improvement in cycle life performance of high capacity nickel-metal hydride battery. *J. Alloys Compd.* **1995**, *231*, 598–603.
41. Kong, L.; Chen, B.; Young, K.; Koch, J.; Chan, A.; Li, W. Effects of Al- and Mn-contents in the negative MH alloy on the self-discharge and long-term storage properties of Ni/MH battery. *J. Power Sources* **2012**, *213*, 128–139.
42. Kim, S.; Chourashiya, M.G.; Park, C.; Park, C. Electrochemical performance of NAFION coated electrodes of hydriding combustion synthesized MgNi based composite hydride. *Mater. Lett.* **2013**, *93*, 81–84.

© 2015 by the authors; licensee MDPI, Basel, Switzerland. This article is an open access article distributed under the terms and conditions of the Creative Commons Attribution license (<http://creativecommons.org/licenses/by/4.0/>).